2020-01-0022

# Application of Extended Messinger Models to Complex Geometries

**Avani Gupta**
Graduate Research Assistant
Georgia Institute of Technology
Atlanta, GA, USA

**Lakshmi N. Sankar**
Regents Professor
Georgia Institute of Technology
Atlanta, GA, USA

**Richard E. Kreeger**
Aerospace Engineer
NASA Glenn Research Center
Cleveland, OH, USA

## ABSTRACT

Since, ice accretion can significantly degrade the performance and the stability of an airborne vehicle, it is imperative to be able to model it accurately. While ice accretion studies have been performed on airplane wings and helicopter blades in abundance, there are few that attempt to model the process on more complex geometries such as fuselages. This paper proposes a methodology that extends an existing in-house Extended Messinger solver to complex geometries by introducing the capability to work with unstructured grids and carry out spatial surface streamwise marching.

For the work presented here commercial solvers such as STAR-CCM+ and ANSYS Fluent are used for the flow field and droplet dispersed phase computations. The ice accretion is carried out using an in-house icing solver called GT-ICE. The predictions by GT-ICE are compared to available experimental data, or to predictions by other solvers such as LEWICE and STAR-CCM+. Three different cases with varying levels of complexity are presented. The first case considered is a commercial transport airfoil, followed by a three-dimensional MS(1)-317 swept wing. Finally, ice accretion calculations performed on a Robin fuselage have been discussed. Good agreement with experimental data, where applicable, is observed. Differences between the ice accretion predictions by different solvers have been discussed.

## INTRODUCTION

Ice accretion poses a major problem for both civilian and military aircraft alike, severely jeopardizing the safety and survivability of the vehicle. The development of analytical and empirical ice tools to understand the ice accretion process is crucial. Existing methodologies, such as the Messinger model employed by LEWICE and FENSAP, are able to predict ice shapes and growth on airframe surfaces relatively well. However, most of the existing studies have been carried out on relatively simple geometries like 2D airfoils and 3D airplane wings and rotor blades.

To understand the ice growth on more complex geometries, such as fuselage and radome, requires the utilization of unstructured meshes to simulate the flow field around these geometries. Following the aerodynamic simulation, the flow field information has to flow to a dispersed water phase calculation tool which can estimate the impingement collection efficiency of the water droplets onto the airframe surface. This then needs to be provided as input, along with flow field information, to the ice accretion codes.

This paper extends an existing extended Messinger ice accretion tool, developed at Georgia Tech called GT-ICE, to interface with solvers utilizing unstructured meshes for flow simulation.

## LITERATURE REVIEW

Several of the existing ice accretion methodologies are based on the classical Messinger model [1]. This model relies on a one-dimensional energy balance approach for the analysis of the conditions which govern the equilibrium temperature of an insulated, unheated surface exposed to icing. It is employed by several industry standard tools such as LEWICE and FENSAP's ICE3D.

FENSAP, developed by Habashi et al. [2-8] is able to use structured, unstructured as well as hybrid meshes for its ice accretion calculations. The droplet code employed by it is called DROP3D, which is a fully-three dimensional Eulerian approach for air flows containing water droplets. The ice accretion module, called ICE3D relies on converting the classical Messinger model into a PDE system of conservation equations, which allows both two-dimensional and three-dimensional calculations to be performed. ICE3D models the formation of film of water on top of the ice accreted, on top of the airframe surface. The shear stress exerted by the external flow field determines the direction of flow for this water film.

Tran et al. [7] employed FENSAP-ICE to study ice accretion on a tiltrotor aircraft. Considering the complex geometry, unstructured grids were used for the simulations. Fouladi et al. [8] carried out ice accretion studies on the Robin fuselage using FENSAP. Significant ice accretion was predicted, near the nose of the fuselage, after an ice accretion time of 30 minutes. Effects of different flow parameters such as forward speed and ambient temperature were also studied.

LEWICE [9-17], an industry standard ice accretion tool developed under the direction of the NASA Glenn Research Center, also employs the classical Messinger model. It uses the panel method for flow field computations, and a Lagrangian particle tracking method for computing the droplet impingement on the airframe surface. An integral

laminar (Thwaites method) and turbulent (Head's method) boundary layer method is used to determine the coefficient of skin friction. Subsequently, the Reynolds analogy is invoked to compute the heat transfer rate at the airframe surface. LEWICE has both two-dimensional and three-dimensional versions. The three-dimensional icing code, LEWICE3D [16], can handle both structured as well as unstructured grid based flow solutions. It can calculate the impingement efficiencies for single droplets or droplet distributions, which are interpolated onto surface streamlines. Finally, the ice accretion is carried out along these surface streamlines.

Bidwell et al. [17] have investigated the application of LEWICE3D to a multitude of geometries such as a swept MS(1)-317 wing, a swept NACA 0012 wing tip, an axisymmetric inlet and a Boeing 737-300 inlet. Results from the MS(1)-317 swept wing case have been used for comparison for one of the studies presented in this paper.

The extended-Messinger model, developed by Myers [18] builds on the classical Messinger model [1]. It brings in the added capability to be able to model the temperature gradients in the ice and the water layers. This approach was utilized by Kim [19] and incorporated in the in-house ice accretion tool developed at Georgia Tech, GT-ICE. Furthermore, Kim et al. coupled the existing ice-accretion analysis with a rotary wing flow-field analysis. This methodology was applied to several 2D airfoil cases, as well as 3D rotor blade cases. One such case studied by Kim is the Bell Helicopter Model 206B Tail Rotor Blade case [20]. A de-icing module, based on thermal de-icing systems, and a shedding module, based on the force-balance approach [19,21] were also developed. Gupta et al. [22] employed a time marching approach, instead of spatial marching, to some 2D steady airfoil cases and an oscillating Sikorsky SC 2110 airfoil case. The work presented in this paper extends Kim's work to the usage of unstructured grids, where the spatial marching process is carried out along surface streamline to include the three-dimensional effects of the flow.

## METHODOLOGY

The methodology adopted for all the cases presented in this paper is highlighted with the help of a flow-chart presented under Figure 1. First the flow field information around the geometry to be tested is obtained. In this paper, commercial software such as STAR-CCM+ and ANSYS Fluent were used for this step. The flow field simulations were all carried out using unstructured meshes. The commercial flow solvers may be swapped out for any unstructured flow solvers such as FUN3D or in-house formulations. For the dispersed phase water droplet simulations, STAR-CCM+ was employed for the cases presented. Alternatively, industry standard tools such as LEWICE or open source codes such as OpenFOAM may also be employed. Both the flow field and droplet collection efficiency information are crucial for determining ice accretion. These are provided as inputs to the in-house ice accretion tool developed at Georgia Tech called GT-ICE [ 20]. For comparison purposes, the ice accretion simulations were also carried out using STAR-CCM+ and LEWICE Version 3.2, hereby referred to as LEWICE. Some cases have experimental icing data available and/or simulated LEWICE3D data and comparisons have been made, where applicable.

GT-ICE employs the Extended Messinger model [18], which builds on the classical Messinger model [1]. The Classical Messinger model uses an energy balance approach to model the ice formation. However, it does not account for the temperature gradients in the ice and the water layers. The Extended Messinger models allows these gradients to be taken into consideration. The approach involves two heat conduction equations, one each for the ice and the water layers (equations 1 and 2), a mass balance equation (equation 3) and a phase change condition (equation 4) at the interface between the ice and the water layers.

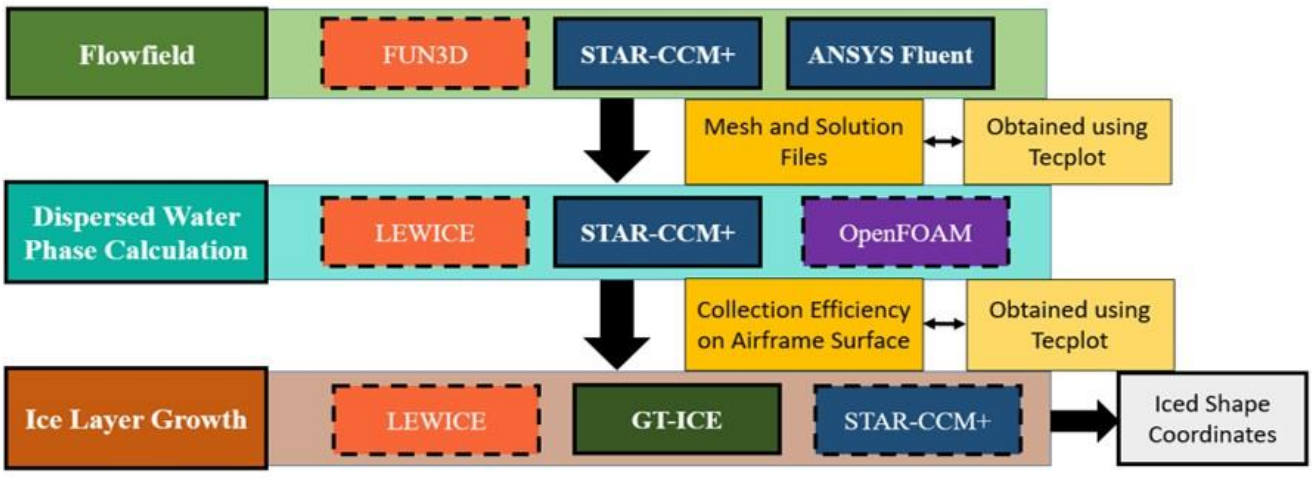


**Figure 1: This figure shows the flow of information along different steps for the process adopted in this paper. The software used for the cases presented here are highlighted with a solid black outline.**

$$\frac{\partial T}{\partial t} = \frac{k_i}{\rho_i C_{pi}} \frac{\partial^2 T}{\partial y^2} \quad (1)$$

$$\frac{\partial \theta}{\partial t} = \frac{k_w}{\rho_w C_{pw}} \frac{\partial^2 \theta}{\partial y^2} \quad (2)$$

$$\rho_i \frac{\partial B}{\partial t} + \rho_w \frac{\partial h}{\partial t} = (LWC)\beta V_\infty + \dot{m}_{in} - \dot{m}_{e,s} \quad (3)$$

$$\rho_i L_F \frac{\partial B}{\partial t} = k_i \frac{\partial T}{\partial t} - k_w \frac{\partial \theta}{\partial t} \quad (4)$$

Here, T represents the temperature in the ice layer and θ represents the temperature in the water layer. $C_{pi}$ and $C_{pw}$ are the values for the specific heats of ice and water, respectively. B is the ice layer thickness, h is the water layer thickness, $\rho_i$ and $\rho_w$ are the densities of ice and water respectively, $k_i$ and $k_w$ are the thermal conductivities of ice and water respectively. β is the collection efficiency, LWC is the freestream Liquid Water Content, $V_\infty$ is the freestream velocity, and $L_F$ is the latent heat of fusion.

Equation 3 represents mass balance, where the terms on the left hand side represent the growth rate of the ice and water layers, respectively. On the right hand side, the first term represents the mass flow rate in due to the droplet impingement, the second term represents the runback mass flow rate in from the upstream cell and the final term represents the mass flow rate out due to evaporation and/or sublimation. A spatial marching process is adopted by GT-ICE, where the stagnation point is first detected and then used as a starting point for the marching. For an airfoil section, the marching occurs both long the upper and the lower sections from the leading edge to the trailing edge. In this paper the methodology has also been extended to be applicable along a streamline, where instead of using a two-dimensional section, the marching is carried out along a three-dimensional streamline. This allows three-dimensional flow to be taken into account when computing ice accretion, and is important for more complex geometries such as a helicopter fuselage.

Figure 2 [22] illustrates the spatial marching process adopted by GT-ICE and the contribution from the different terms in the mass balance equation.

## RESULTS AND DISCUSSION

For the cases presented under this section, STAR-CCM+ was used for the flow field simulations for the commercial transport airfoil case and for the MS(1)-317 swept wing case. ANSYS Fluent was utilized for the calculations for the Robin fuselage case. To compute the droplet impingement rate, STAR-CCM+'s Dispersed Multi-Phase (DMP) simulation [23] was used for all the three cases presented.

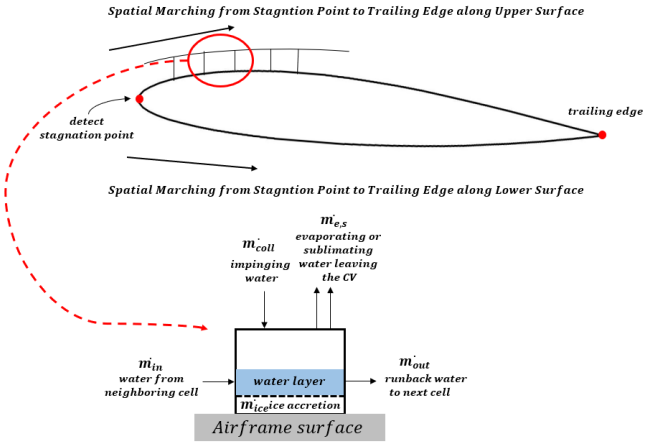


**Figure 2: Illustration of the spatial marching methodology adopted by GT-ICE [22].**

For STAR-CCM+'s flow field simulations, a steady-implicit solver was used. For modeling the effects of turbulence, the K-epsilon turbulence model [24, 25] was used employed.

For ANSYS Fluent's flow field simulation, again a steady-implicit solver was used. However, the 1 equation Spalart-Allmaras [26] model was used for turbulence. The spatial discretization was carried out using a third order MUSCL scheme for the flow.

The Dispersed Multi-Phase (DMP) simulations, carried out in STAR-CCM+, were unsteady owing to the nature of the flow, therefore, an unsteady-implicit solver was used. The temporal discretization was first order. A separate set of conservation equations for a thin film of water on the wing/fuselage surface was solved. It was assumed that this water film had a constant density. For the dispersed phase water droplets, the interaction between the water droplets and the continuum was defined by the drag force and heat transfer. The drag coefficient on the water droplets was calculated using the Schiller-Naumann [27] method and the heat transfer coefficient was calculated using the Ranz-Marshall [28] method. Interaction between the dispersed phase water droplets and the water film occurred through impingement only.

### Commercial Transport Airfoil Case

The first case that is presented is a 2D commercial transport airfoil case. The flow field and icing analysis in STAR-CCM+ was carried out as a three-dimensional simulation, where the airfoil was modeled as an infinite span wing. The results presented were all analyzed at mid-span. The unstructured mesh was generated using the meshing tools available in STAR-CCM+. The final fluid domain had a total of 28,428 cells out of which a majority of the cells were hexahedral with some tetrahedral, prismatic and polyhedral cells as well. This has been shown in Figure 3a. Figure 3b shows the refined mesh close to the wing surface. The surface mesh has a total of 1,218 cells.

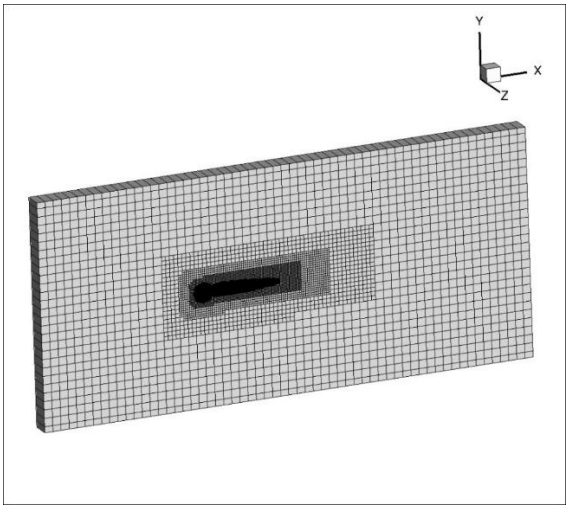


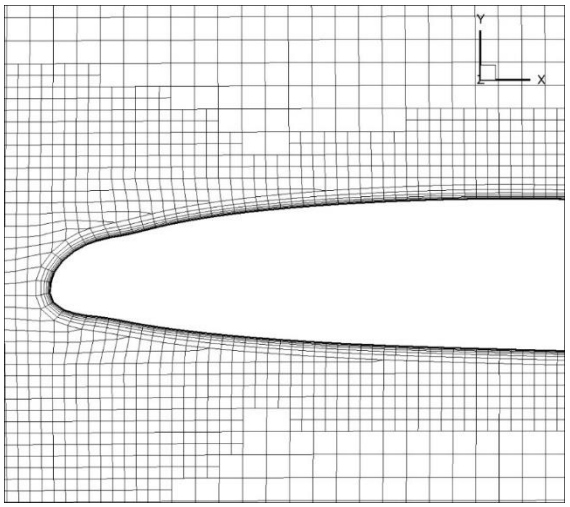


**Figure 3: Figure 3a (top) shows the full fluid domain for the airfoil case. Figure 3b (bottom) shows the mesh close to the airfoil surface. The mesh was generated using STAR-CCM+.**

The flow field parameters have been summarized under Table 1. The coefficient of pressure and the coefficient of skin friction as a function of the x distance along the airfoil have been presented under Figures 4a and 4b respectively. Since, there is a small angle of attack of 0.7°, and since the airfoil is cambered, a finite lift is being generated as may be seen in Figure 4a.

The droplet impingement rate obtained using STAR-CCM+'s Dispersed Multi Phase simulation has been shown in Figure 5. It may be seen that the largest values of the impingement rate are observed close to the leading edge and are close to 0.03 $Kg/m^2s$. Away from the leading edge, no droplet impingement is observed on the rest of the wing.

**Table 1: This table shows the flow characteristic values for the commercial transport airfoil case studied.**

| Property | Value |
|---|---|
| Static Temperature (K) | 258.4 |
| Freestream Velocity (m/s) | 129 |
| LWC ($g/m^3$) | 0.341 |
| MVD (m) | 21e-6 |
| Chord Length (m) | 0.91 |
| Total Spray Time (s) | 342 |
| Angle of Attack (°) | 0.7 |

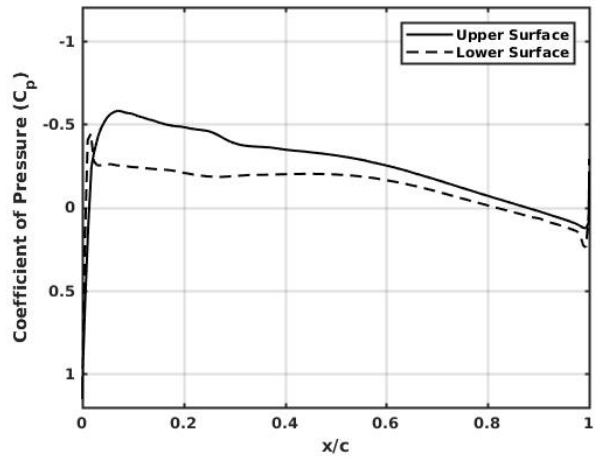


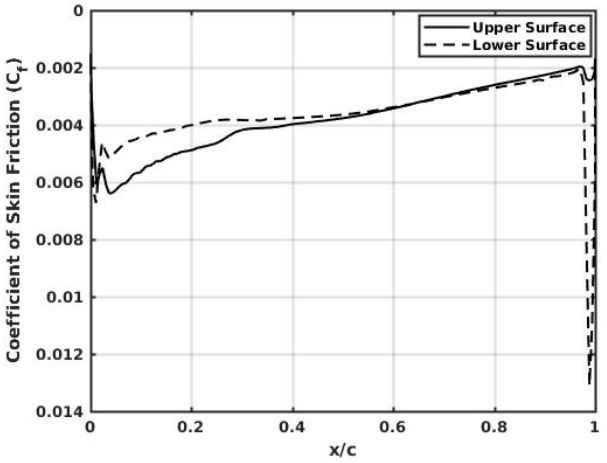


**Figure 4: Figure 4a (top) shows the coefficient of pressure. Figure 4b (bottom) shows the coefficient of skin friction. Both have been plotted as a function of the non-dimensional x distance along the airfoil.**

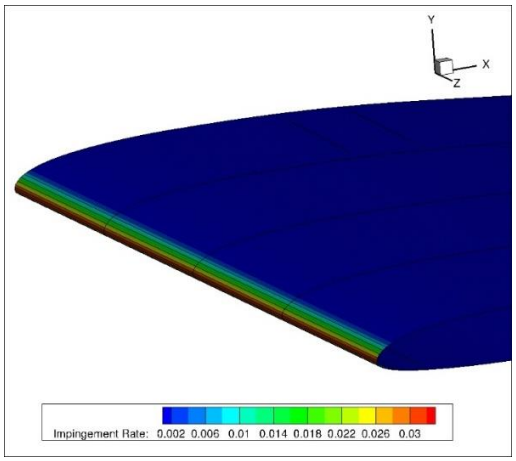


**Figure 5: This figure represents the impingement rate, in Kg/m$^2$s, obtained on the surface of the infinite span wing. The highest values are observed close to the leading edge.**

This droplet impingement rate is normalized by the freestream Liquid Water Content (LWC) and the freestream velocity to yield the non-dimensional droplet collection efficiency. This has been plotted as a function of the non-dimensional surface wrap distance where the surface wrap starts at the trailing edge, moves to the leading edge along the lower surface of the wing section and then back to the trailing edge along the upper surface. Figure 6 shows the comparison between the values of the collection efficiency obtained using STAR-CCM+ and LEWICE. It is seen that both the programs predict similar values close to the leading edge, with a peak value of around 0.72.

The coefficient of pressure, coefficient of skin friction and the collection efficiency values computed using the unstructured mesh set-up in STAR-CCM+ are provided as inputs to GT-ICE. The ice shape obtained using GT-ICE has been compared to those obtained using LEWICE and STAR-CCM+.

Figure 7 shows the ice shape results obtained at the end of 60 seconds of ice accretion time. GT-ICE and LEWICE predict similar maximum ice thickness. This is thicker than what is being predicted by STAR-CCM+. The results obtained at the end of the full 342 seconds have been plotted in Figure 8. The results have also been compared to the experimental data available [29]. The experimental tests were conducted at the NASA Lewis Icing Research Tunnel (IRT).

GT-ICE and LEWICE predict thicker ice shapes, consistent with the result at the end of 60 seconds, as compared to STAR-CCM+ and the experimental data. The difference in the predicted thickness may be attributed to the flow field characteristics used for the icing simulation. For GT-ICE, the aerodynamic simulation was carried out as a single step process i.e. the initial clean airfoil results were used for modeling the full 342 seconds of ice accretion. Similarly, the simulation using LEWICE was performed using six steps, which means six flow field updates, however, STAR-CCM+ runs an unsteady, coupled aerodynamic and icing simulation. Despite the single step flow field update, the extents of the ice shape precited by GT-ICE match well with experimental data.

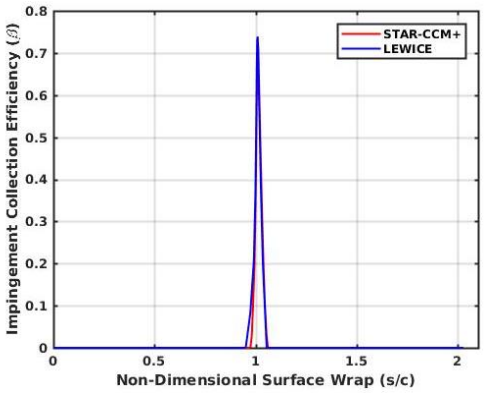


**Figure 6: This figure compares the collection efficiency values obtained, for the commercial transport airfoil case, from the DMP STAR-CCM+ simulation and LEWICE.**

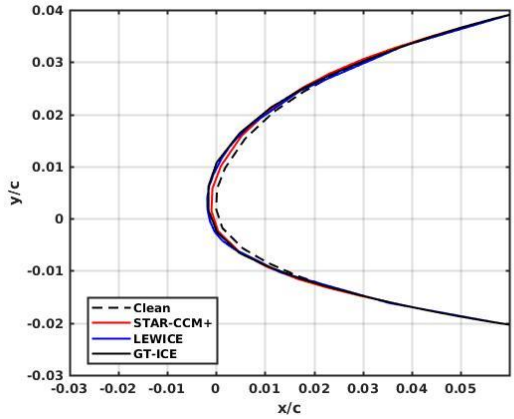


**Figure 7: This figure compares the ice accretion predicted on the airfoil by STAR-CCM+, LEWICE and GT-ICE at the end of 60 seconds.**

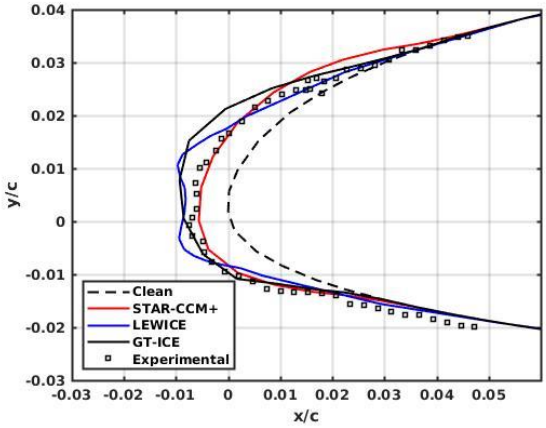


**Figure 8: This figure compares the ice shape predicted by STAR-CCM+, LEWICE and GT-ICE, with experimental data, at the end of 342 seconds.**

## MS(1)-317 Swept Wing Case

The second case that was studied was a swept wing case, with a MS(1)-317 airfoil section. The wing had a sweep angle of 30°, a chord length of 3ft and a span of 6ft. The wing geometry used for the mesh has been shown in Figure 9. Figure 10 shows the clean MS(1)-317 airfoil section used for the wing. The case was chosen due to the availability of experimental collection efficiency data on the 3D wing model [17]. Experimental ice accretion data was not available, however, some predicted ice shapes results using LEWICE3D [16] were available, which have been used for comparison. The tests were conducted in the NASA Lewis Icing Research Tunnel (IRT). For the impingement efficiency testing, the IRT utilizes a dye tracer technique. Following this, the location and the amount of water impinging on the model can be measured. Please note that experimental spray time specification is not available.

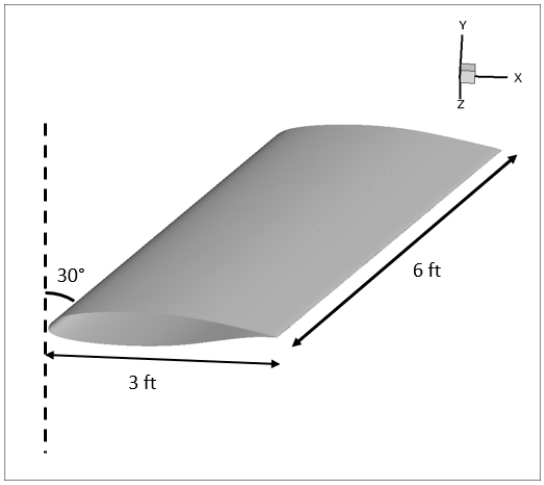


**Figure 9: This figure represents the geometry for the MS(1)-317 swept wing case. The sweep angle is 30°.**

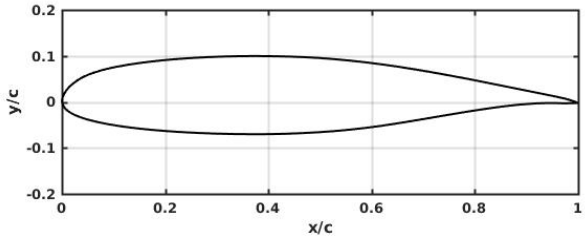


**Figure 10: This figure represents the shape of the MS(1)-317 airfoil, used as a section for the swept wing case.**

The full fluid domain has been pictured in Figure 11a. It extends around 12 chord lengths in the streamwise and normal directions. An attempt to model the wing tip effects was not made, in accordance with the original simulation which was performed using LEWICE3D. The fluid domain consisted of a total of 502,505 cells. Around 80% of the cells were hexahedral, with 20% tetrahedral, prismatic and polyhedral cells. There were 15,008 cells on the wing surface, pictured in Figure 11b. Out of these 11,117 were quadrilateral with some triangular and polyhedral cells. The mesh refinement adopted close to the wing surface has been illustrated in Figure 11c.

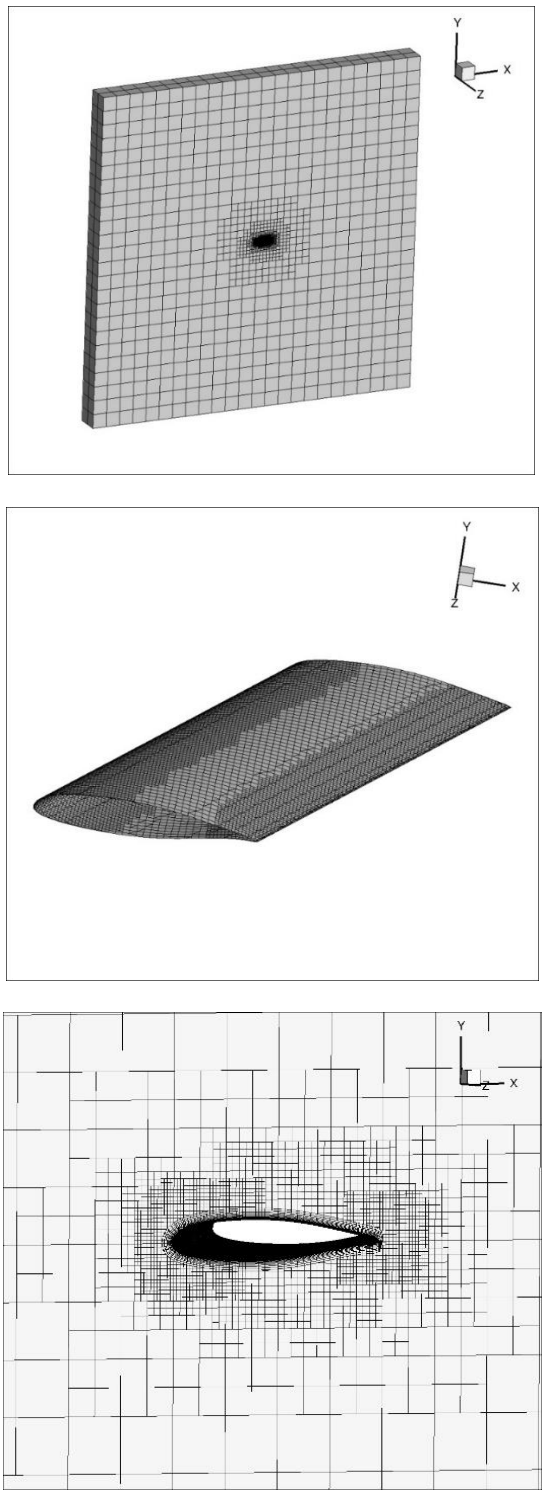


**Figure 11: Figure 11a (top), shows the full fluid domain created for the swept wing icing case, figure 11b (center) shows the surface mesh for the wing and figure 11c (bottom) shows the mesh close to the wing surface. The mesh was generated using STAR-CCM+.**

For this case, the experimental data available for the collection efficiency values was for a certain set of flow characteristics, listed under Table 2. Two different ice accretion studies were performed, one at 0° angle of attack and the other at 8° angle of attack. The flow characteristics corresponding to each case have been listed under Tables 3 and 4, respectively.

**Table 2: This table shows the flow characteristics for the collection efficiency comparison case for the swept wing.**

| Property | Value |
|---|---|
| Static Temperature (K) | 281.15 |
| Freestream Velocity (m/s) | 75 |
| LWC (g/m$^3$) | 0.4 |
| MVD (m) | 20e-6 |
| Chord Length (m) | 0.91 |
| Total Spray Time (s) | 1800 |
| Angle of Attack (°) | 0.0 |

**Table 3: This table shows the flow characteristic values for the ice accretion comparison case with 0° AoA for the swept wing.**

| Property | Value |
|---|---|
| Static Temperature (K) | 263.85 |
| Freestream Velocity (m/s) | 75 |
| LWC (g/m$^3$) | 0.695 |
| MVD (m) | 20e-6 |
| Chord Length (m) | 0.91 |
| Total Spray Time (s) | 1800 |
| Angle of Attack (°) | 0.0 |

Figure 12 shows the comparison between the experimental collection efficiency values and those predicted by LEWICE3D and STAR-CCM+'s Dispersed Multi Phase (DMP) simulation. The experimental values have a much higher peak value of 0.6 as opposed to the predicted values, which are close to 0.4. One reason for this discrepancy is the Liquid Water Content (LWC) value that was used for normalization. For the experimental results, the local LWC value was used. This was measured at each blotter strip location on the model wing. The technique involves spraying a dye-water solution of known concentration onto the model covered with blotter stripes and the local impingement rate is reflected as a variation in color intensity [17]. However, for both LEWICE3D and STAR-CCM+, the freestream LWC value was used since no information for the local LWC values was available. For the extents of the collection efficiency, it may be seen that LEWICE3D overestimates the wetted surface area on the wing, whereas STAR-CCM+ underestimates the wetted surface area on the lower surface, as compared to the experiment. On the upper surface, between surface wrap values of around 2 cm to 8 cm, STAR-CCM+ has good agreement with the experimental data, with perfect agreement close to a surface wrap distance value of 5 cm.

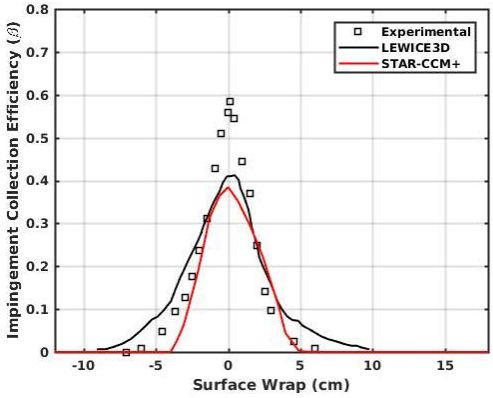


**Figure 12: This figure shows the comparison between the impingement collection efficiency values observed experimentally, and those predicted by LEWICE 3D and STAR-CCM+.**

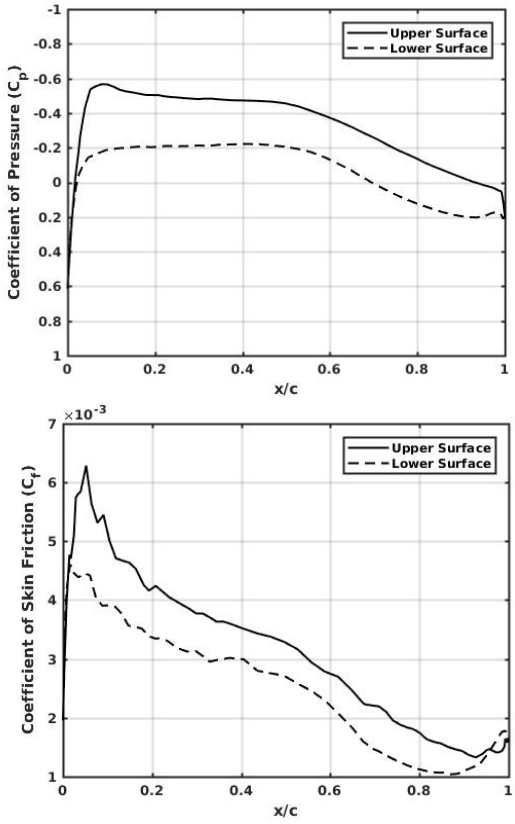


**Figure 13: Figure 13a (top) shows the coefficient of pressure. Figure 13b (bottom) shows the coefficient of skin friction. Both have been plotted as a function of the non-dimensional x distance along the clean swept wing at mid-span for the ice accretion case, with an AoA of 0°.**

Presented in Figures 13a and 13b are the coefficients of pressure and skin friction obtained from the flow field STAR-CCM+ simulation. The results have been plotted at mid-span, section normal to the wing leading edge, because of the availability of LEWICE3D ice accretion data at this location. The wing generates finite lift, even at 0° angle of attack because of the cambered MS(1)-317 section. The coefficient of lift predicted by the simulation is close to 0.2562 and the coefficient of drag is close to 0.009545.

Figure 14 represents the droplet collection efficiency values obtained for the ice accretion case, at mid-span, using STAR-CCM+. Similar to the previous case, peak values close to 0.39 are observed close to the leading edge. These collection efficiency values, along with flow field information such as coefficient of pressure and coefficient of skin friction, obtained from STAR-CCM+ are provided as inputs to GT-ICE.

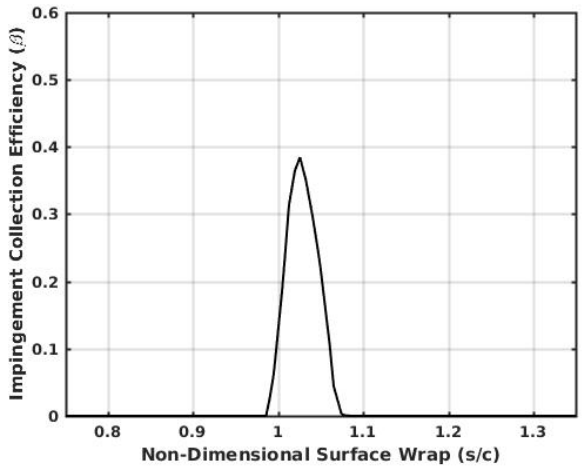


**Figure 14: This figure shows the collection efficiency values obtained using STAR-CCM+ for the first ice accretion case. These values are plotted as a function of the non-dimensional surface wrap distance.**

Figure 15 shows the ice shape predicted by LEWICE3D, GT-ICE and STAR-CCM+, at the end of an icing time of 30 minutes. GT-ICE and STAR-CCM+ predict very similar ice shapes with similar maximum thickness. STAR-CCM+ predicts slightly higher runback on the upper surface, compared to GT-ICE. Both of these predictions differ from the LEWICE3D predictions in terms of the absence of the double ice horn formation (shown by the blue dots). Looking at the collection efficiency values in Figure 12 and the coefficient of skin friction values in Figure 13, most of the ice accretion is expected to occur very close to the leading edge. This is because of the peak collection efficiency values as well as large coefficient of skin friction values and consequently, large coefficient of heat transfer values, close to the leading edge. LEWICE3D also predicts significantly higher runback on the lower surface. This follows from the collection efficiency values comparison shown in Figure 12, where LEWICE3D predicts a higher wetted surface area on the wing. The thickness of the ice formation, close to the leading edge, is similar for all the three solvers.

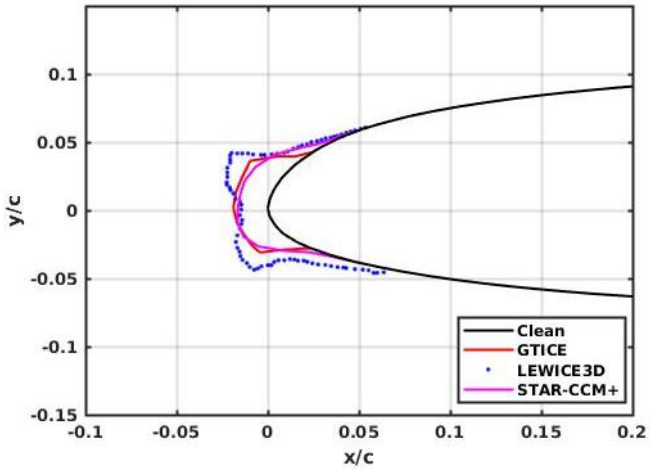


**Figure 15: This figure shows the ice shape predicted by GT-ICE, STAR-CCM+ and LEWICE3D for the ice accretion swept wing case, at an angle of attack of 0°.**

Presented next is the icing case, with a higher angle of attack of 8°.

**Table 4: This table shows the flow characteristic values for the ice accretion comparison case with 8° AoA for the swept wing.**

| Property | Value |
|---|---|
| Static Temperature (K) | 263.85 |
| Freestream Velocity (m/s) | 75 |
| LWC ($g/m^3$) | 0.695 |
| MVD (m) | 20e-6 |
| Chord Length (m) | 0.91 |
| Total Spray Time (s) | 1800 |
| Angle of Attack (°) | 8.0 |

Figures 16a and 16b show the coefficient of pressure and the coefficient of skin friction values at mid-span for the 8° angle of attack case. As may be seen from the coefficient of pressure plot in Figure 16a, significantly higher lift is being generated for this case and the coefficient of skin friction values observed close to the leading edge are also around an order of magnitude higher compared to the 0° angle of attack case. The coefficient of lift, predicted for this case, is close to 0.7911 and the coefficient of drag is close to 0.030535. The incremental rise in the drag coefficient occurs as a result of both increased lift-induced drag as well as increased skin friction drag.

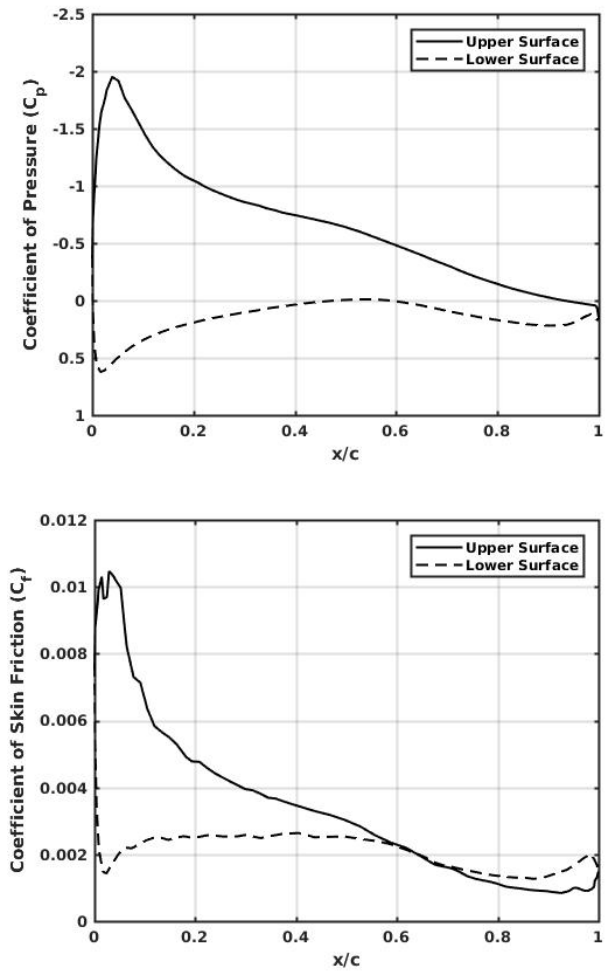


**Figure 16: Figure 16a (top) shows the coefficient of pressure. Figure 16b (bottom) shows the coefficient of skin friction. Both have been plotted as a function of the non-dimensional x distance along the clean swept wing at mid-span for the first ice accretion case, with an angle of attack of 8°.**

Figure 17 shows the collection efficiency values as a function of the non-dimensional surface wrap distance at mid-span. For this case, the distribution is biased towards the lower surface of the wing which sees more droplet impingement. However, the peak value here is around 0.32 which lower than the 0° angle of attack value of 0.39.

Figure 18 shows the ice shape comparisons for LEWICE3D, GT-ICE and STAR-CCM+, at the end of an icing time of 30 minutes. For this case with a higher angle of attack, more ice accretion is observed on the lower surface of the wing. LEWICE3D predicts a double ice horn for this case as well, which is not predicted by either GT-ICE or STAR-CCM+. However, the pointed ice horn formation beneath the leading edge is being predicted by GT-ICE. The thickness of the ice accretion predicted by GT-ICE in this region with x/c close to -0.02 is smaller than that of LEWICE3D. This difference could be arising from smaller collection efficiency values predicted by STAR-CCM+, which are used as inputs for GT-ICE. GT-ICE does predict thicker ice, more in accordance with the prediction by LEWICE3D at around x/c value of 0.02. This may again be attributed to the collection efficiency values, which are similar for both the LEWICE3D and STAR-CCM+ predictions at the peak values.

STAR-CCM+ predicts more runback on the upper surface, as compared to GT-ICE. On the lower surface, both GT-ICE and STAR-CCM+ significantly underpredict the runback, compared to LEWICE3D, in keeping with the collection efficiency trend observed under Figure 12.

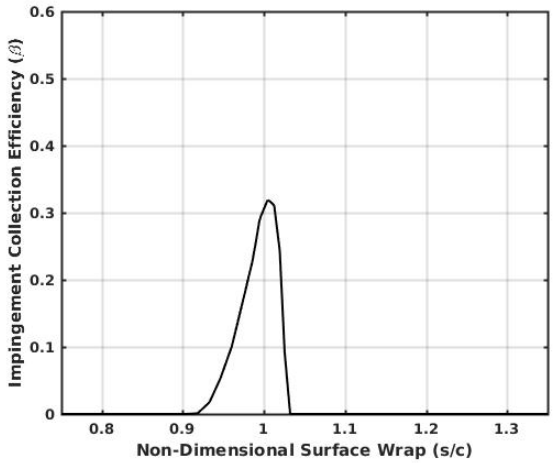


**Figure 17: This figure shows the collection efficiency values obtained using STAR-CCM+ for the second ice accretion case. These values are plotted as a function of the non-dimensional surface wrap distance.**

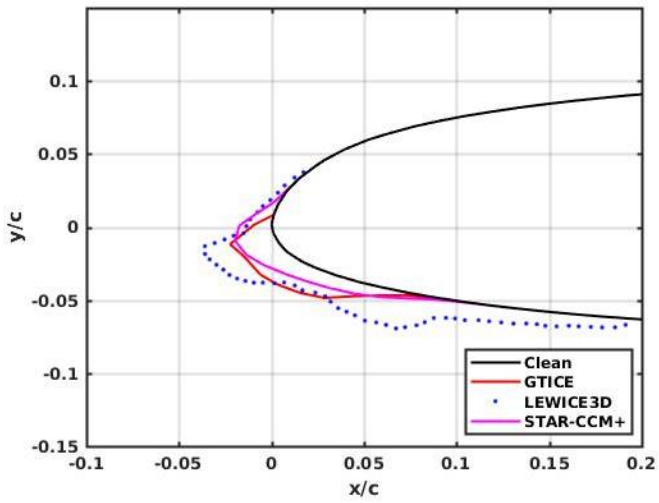


**Figure 18: This figure shows the ice shape predicted by GT-ICE, STAR-CCM+ and LEWICE3D for the second ice accretion swept wing case, at an angle of attack of 8°.**

## Robin Fuselage Case

The final case presented is that of the Robin fuselage. For this case, experimental results are only available for flow field validation [30]. The experiments were carried out in the Langley VSTOL tunnel and the surface pressure measurements, used for flow field validation, were measured using six pressure transducers. No collection efficiency or icing data is available. However, this case serves as a proof of concept that the current extended-Messinger methodology can be extended to complex geometries such as a helicopter fuselage. Figures 19a and 19b show the surface mesh used for this case. The length of the fuselage from the nose to the tip is 3.15 m, and the surface mesh has a total of 34,888 triangular cells. The full fluid domain is of spherical shape, which has a radius of around 15 fuselage lengths. It has a total of 792,309 tetrahedral cells.

The flow field for this case was simulated using ANSYS Fluent, however, STAR-CCM+'s DMP simulation was used to obtain the droplet impingement rates on the fuselage. The effects of rotor down wash were not considered for this case. The left column under Table 5 lists the flow characteristics for the flow field validation case. The freestream velocity is 42 m/s for a relatively low Mach number of 0.12. The right column lists the flow field conditions that were chosen for the ice accretion study. Since, no experimental data is available for validation, appropriate values for the static temperature, the Liquid Water Content (LWC) and the Mean Volume Diameter (MVD) were chosen to facilitate the validation of the unstructured grid methodology.

Figures 20 and 21 show the surface contours for the coefficient of skin friction, the coefficient of pressure, the droplet impingement rate and the Mach number on the fuselage surface. As is expected, the area close to the nose of the fuselage sees the highest values for the impingement rate and the skin friction coefficient (Figure 21), making it most susceptible to ice accretion.

Presented under Figure 22 are the comparisons for the pressure coefficient between the ANSYS simulation and the experimental data at different axial locations along the length of the fuselage. It may be observed that for the most part, there is excellent correlation between the experimental and the simulated values.

Figure 23 shows the predicted ice accretion close to the fuselage nose, both by GT-ICE and STAR-CCM+. GT-ICE predicts thicker ice shape than does STAR-CCM+, however the shapes predicted by both solvers are relatively similar. Negligible ice accretion was predicted close to the hub and no ice accretion was predicted on other areas of the fuselage. For this case, a spatial march along a surface streamline direction as opposed to a 2D section cut was also performed. The surface streamlines on the fuselage were visualized using Tecplot and have been shown in Figure 24.

**Table 5: This table shows the flow characteristic values for the flow field comparison case (left) and the ice accretion case (right) for the Robin fuselage.**

| Property | Value | Value |
|---|---|---|
| Static Temperature (K) | 288.15 | 258.15 |
| Freestream Velocity (m/s) | 42 | 40 |
| Freestream Mach | 0.123 | 0.123 |
| LWC ($g/m^3$) | 2.0 | 2.0 |
| MVD (m) | 20e-6 | 20e-6 |
| Fuselage Length 'L' (m) | 3.15 | 3.15 |
| Angle of Attack (°) | 0.0 | 0.0 |
| Total Spray Time (s) | NA | 180 |

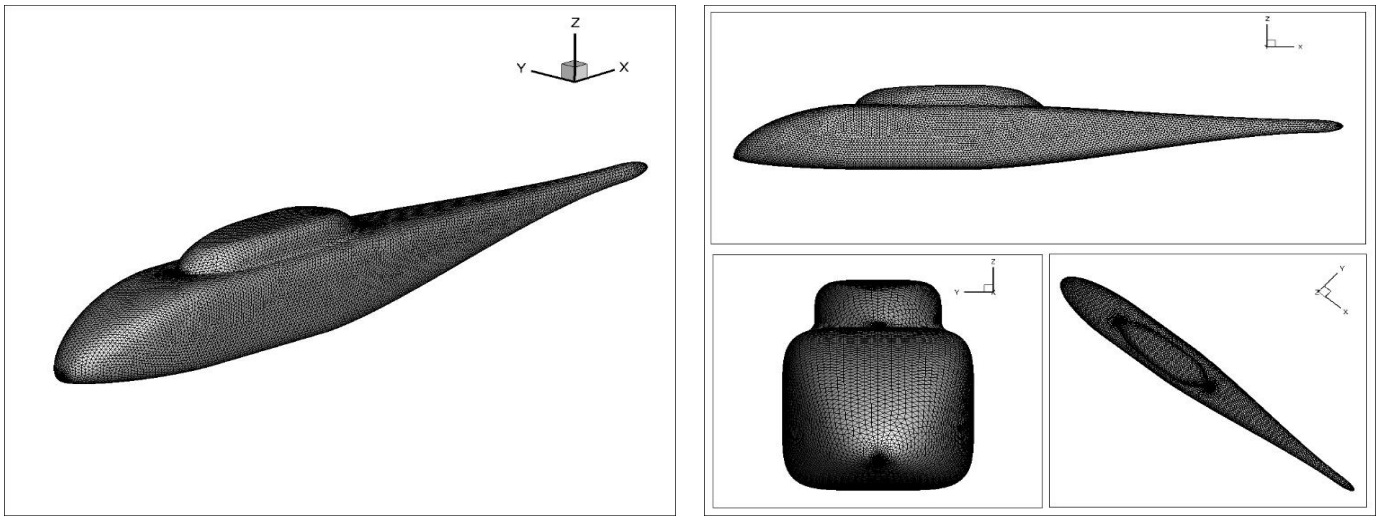


**Figure 19: Figure 19a shows the surface mesh for the Robin fuselage. Figure 19b shows the same surface mesh from a side, front and top down view.**

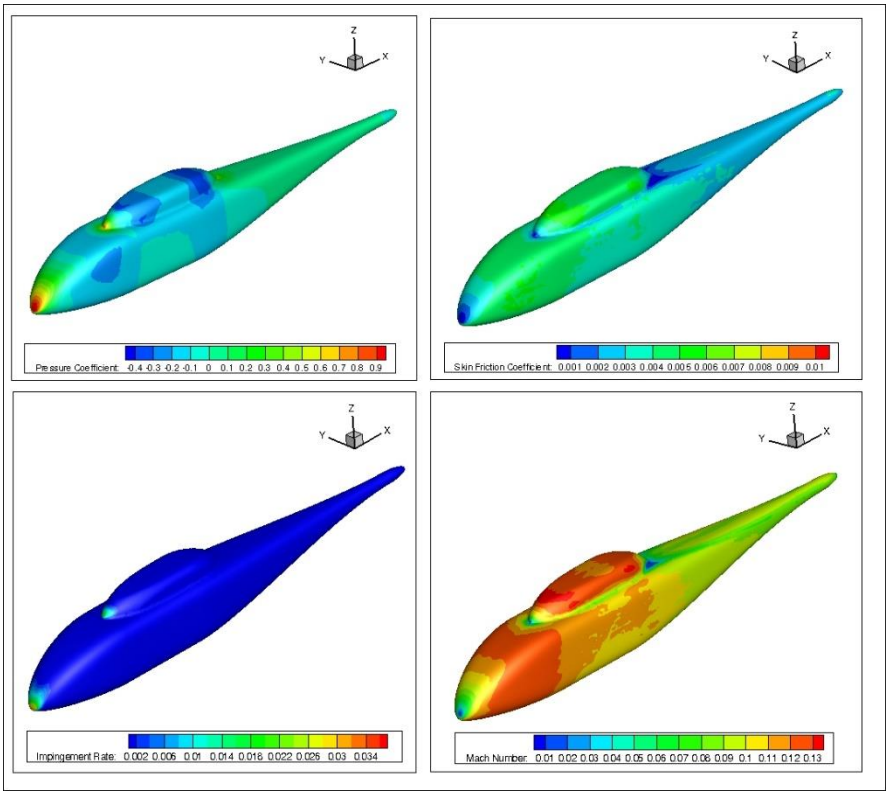


**Figure 20: Surface contour plots for the Pressure Coefficient (top left), Skin Friction Coefficient (top right), Droplet Impingement Rate (bottom left), and the Mach number (bottom right) on the Robin Fuselage.**

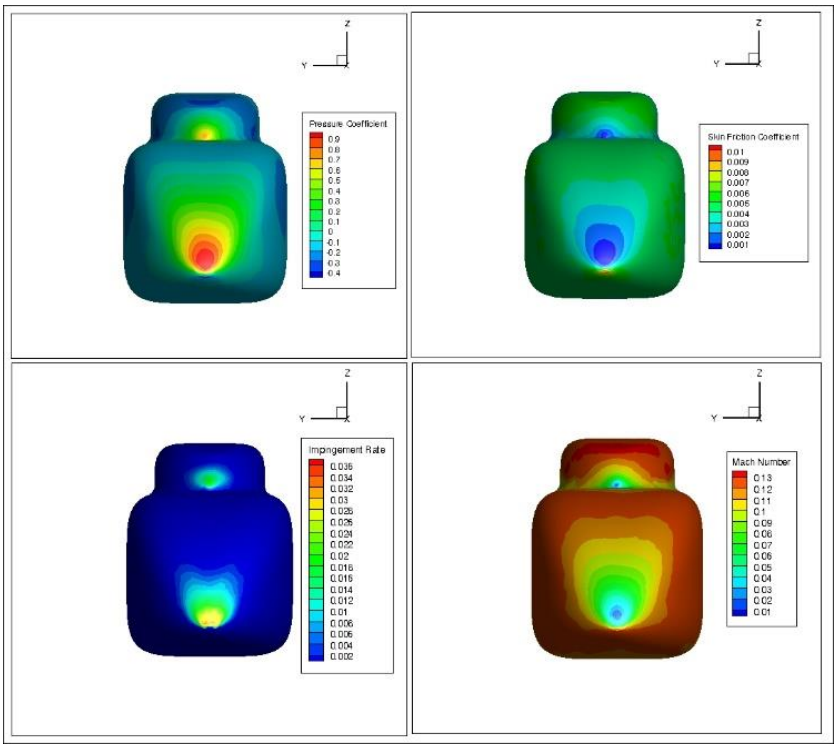


**Figure 21: Surface contours for the Pressure Coefficient (top left), Skin Friction Coefficient (top right), Droplet Impingement Rate (bottom left) and the Mach number (bottom right) around the nose of the Robin fuselage.**

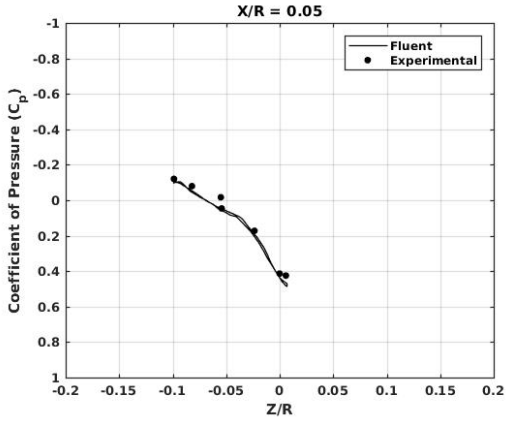
X/R = 0.05
Fluent
Experimental
Coefficient of Pressure (Cp)
Z/R

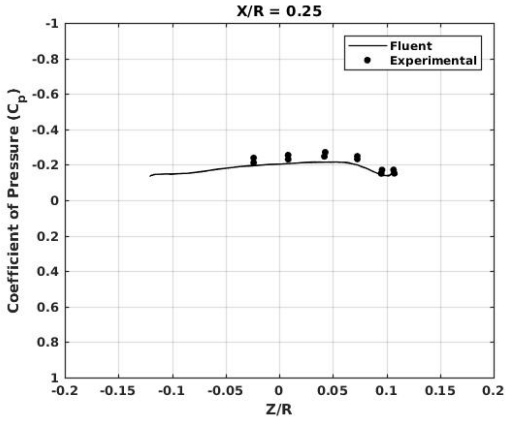
X/R = 0.25
Fluent
Experimental
Coefficient of Pressure (Cp)
Z/R

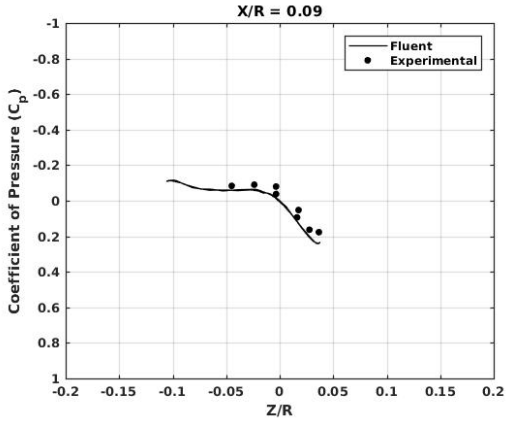
X/R = 0.09
Fluent
Experimental
Coefficient of Pressure (Cp)
Z/R

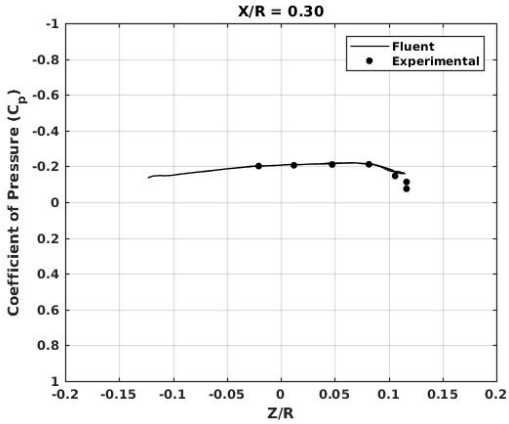
X/R = 0.30
Fluent
Experimental
Coefficient of Pressure (Cp)
Z/R

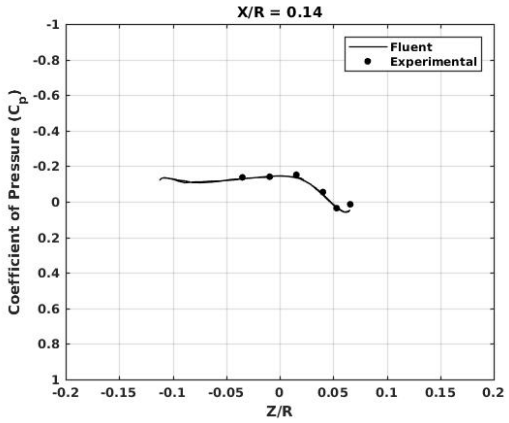
X/R = 0.14
Fluent
Experimental
Coefficient of Pressure (Cp)
Z/R

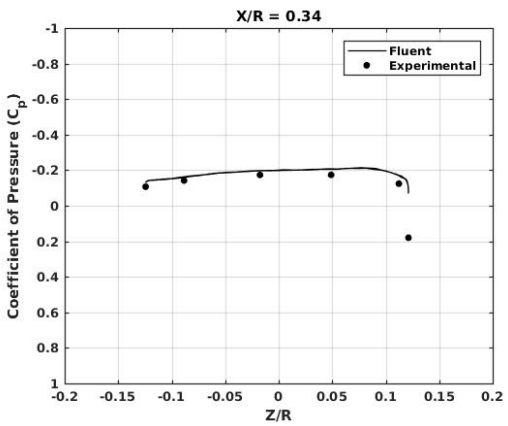
X/R = 0.34
Fluent
Experimental
Coefficient of Pressure (Cp)
Z/R

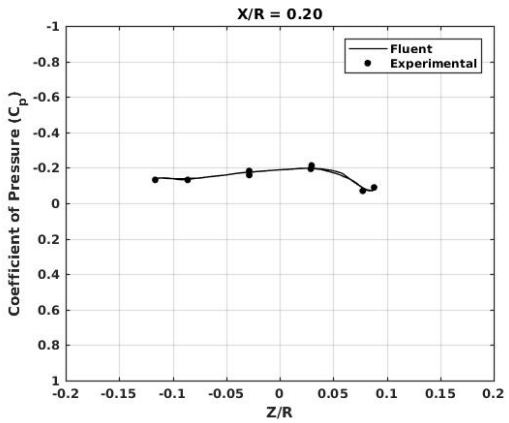
X/R = 0.20
Fluent
Experimental
Coefficient of Pressure (Cp)
Z/R

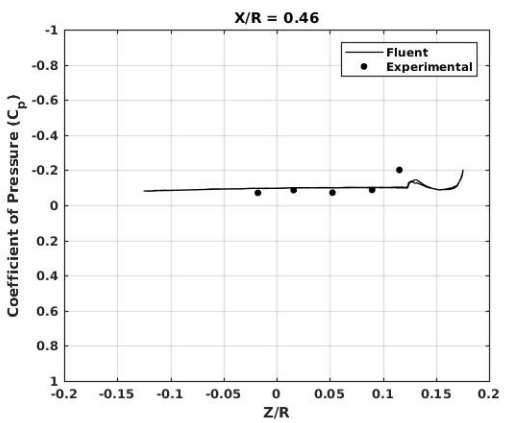
X/R = 0.46
Fluent
Experimental
Coefficient of Pressure (Cp)
Z/R

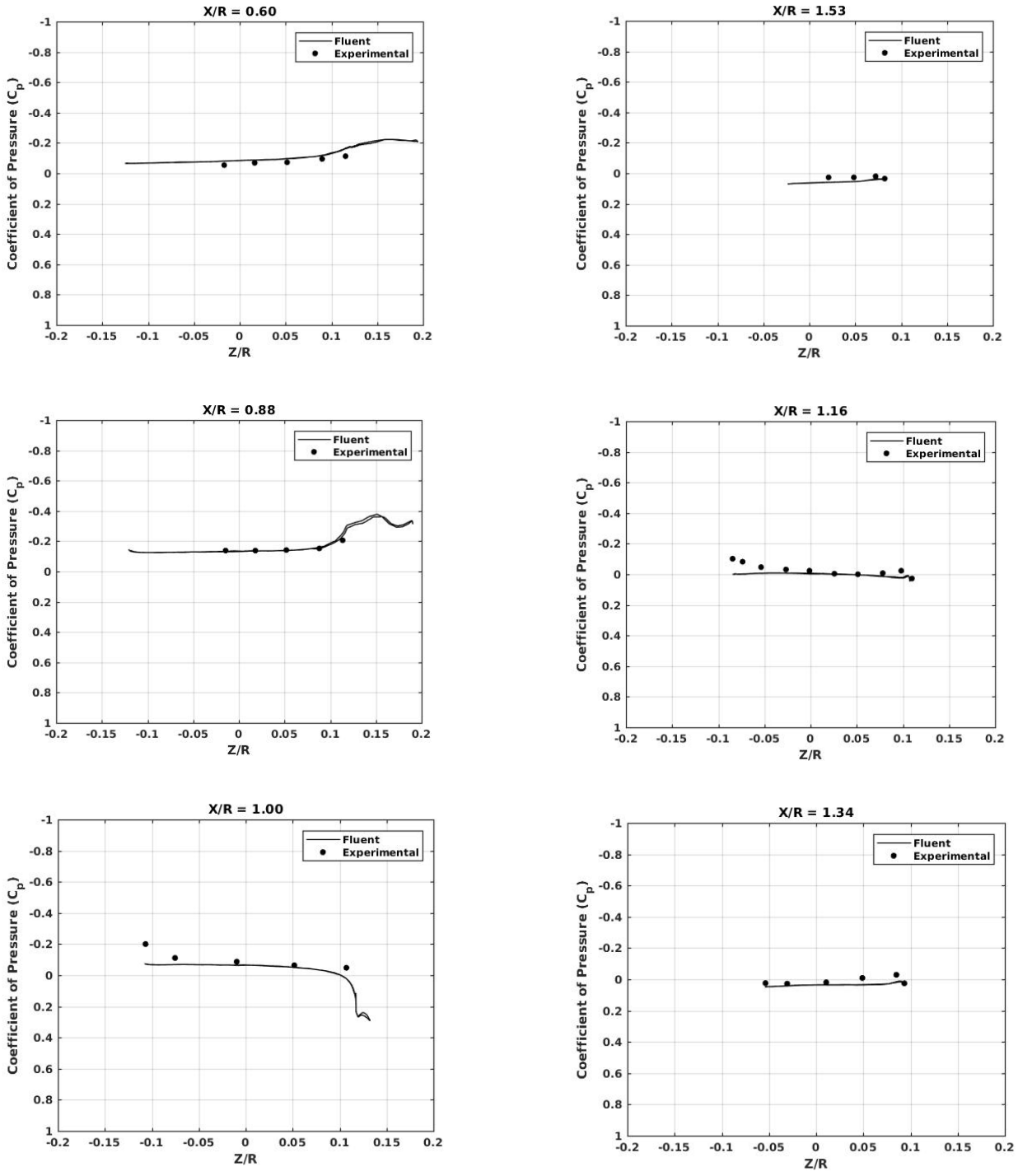


**Figure 22: These figures present the comparison between the Coefficient of Pressure values obtained using ANSYS Fluent and the experimental data at various sections along the x axis of the Robin fuselage.**

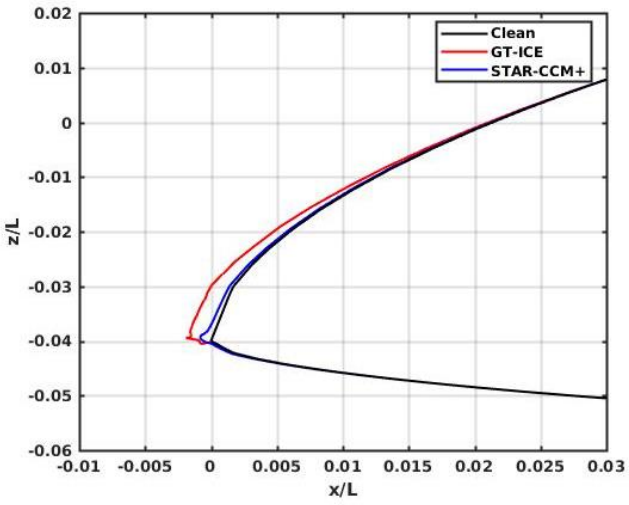


**Figure 23: This figure shows the ice shape predicted by STAR-CCM+ and GT-ICE close to the nose of the Robin Fuselage, at mid-section.**

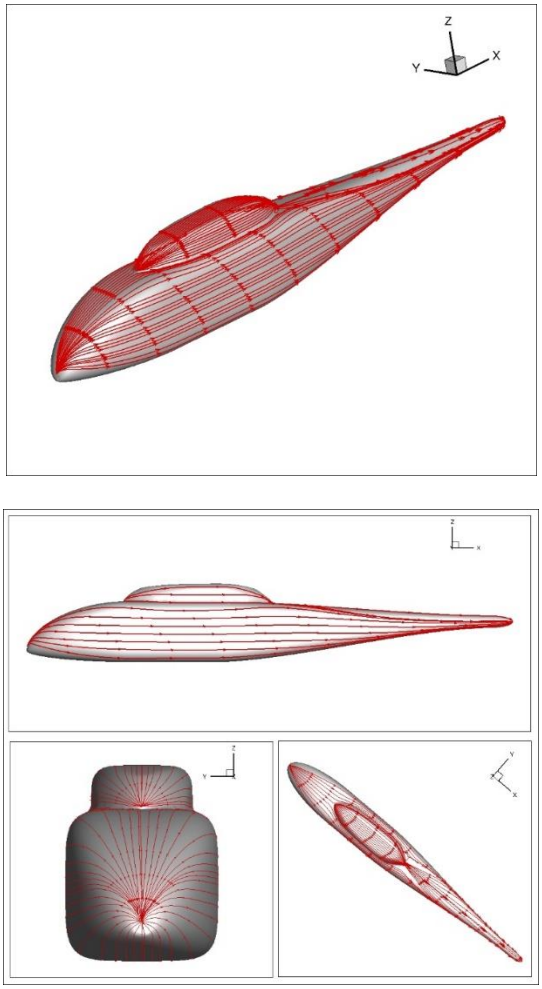

**Figure 24: Surface flow streamlines, visualized using Tecplot, on the Robin fuselage.**

Nine surface streamlines were picked for the validation and ice accretion studies were performed along each of these streamlines.

To obtain the flow field variable values and the impingement rate values along these streamlines, data interpolation using Tecplot [31] was performed. The Inverse-Distance algorithm was used.

Figure 25 shows these nine surface streamlines. Plots under Figure 26 present the coefficient of skin friction, the coefficient of pressure and the impingement collection efficiency along the dimensional surface wrap distance, which starts at the nose of the fuselage, as picturized in Figure 26. Figure 27 shows the predicted ice thickness along each streamline. As may be seen from the plots, ice accretion only takes place close to the fuselage nose. Everywhere else, the ice accretion thickness is either zero or negligible. This follows from the values of the droplet impingement efficiency obtained from the STAR-CCM+ DMP simulation. The collection efficiency values are non-zero for only about 0.3 m, along the surface wrap distance starting at the nose, after which they are consistently close to 0.

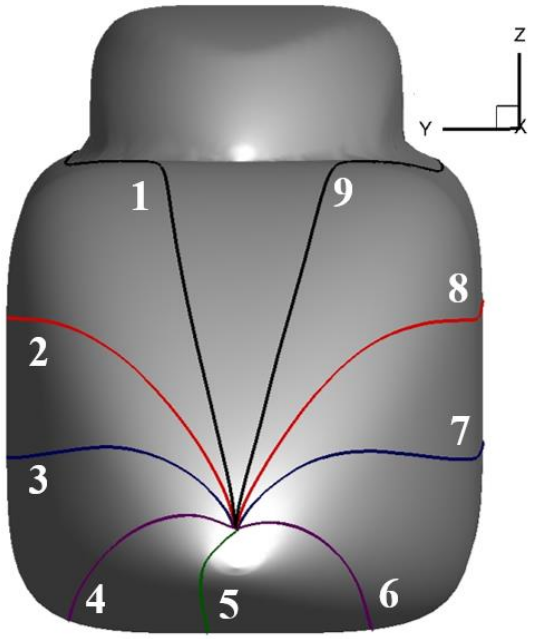


**Figure 25: Pictorial representation of the nine streamlines chosen for the GT-ICE ice accretion calculations.**

Shown under Figure 28, are the three-dimensional views of the ice accretion along each streamline. The figure on the left is a side view of the fuselage nose and the figure on the right is a top down view.

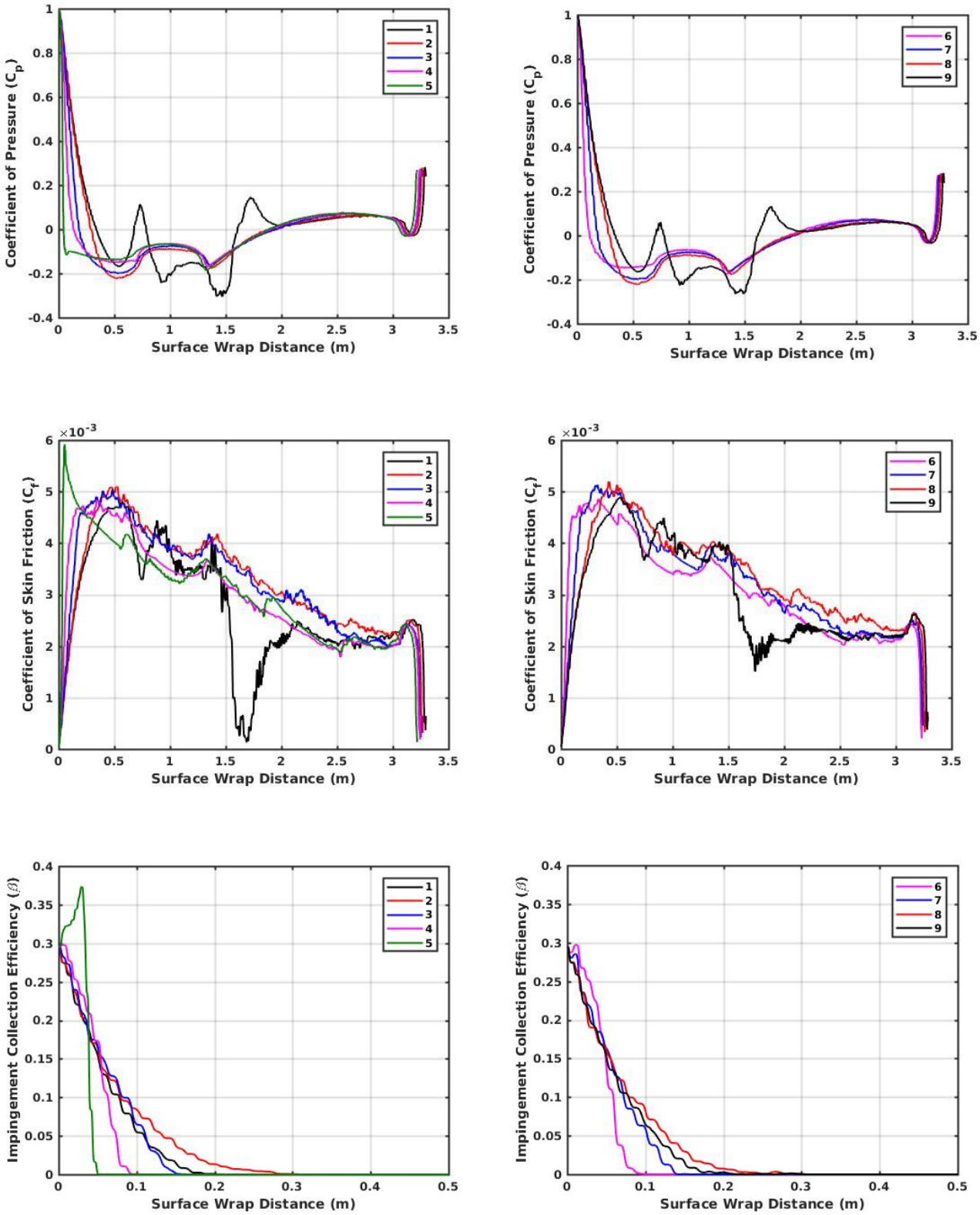


**Figure 26: Flow parameters such as the coefficient of pressure (top row), the coefficient of skin friction (center row) and the droplet impingement collection efficiency (bottom row) as a function of the surface warp distance, starting at the fuselage nose, for the nine streamlines labeled under Figure 25.**

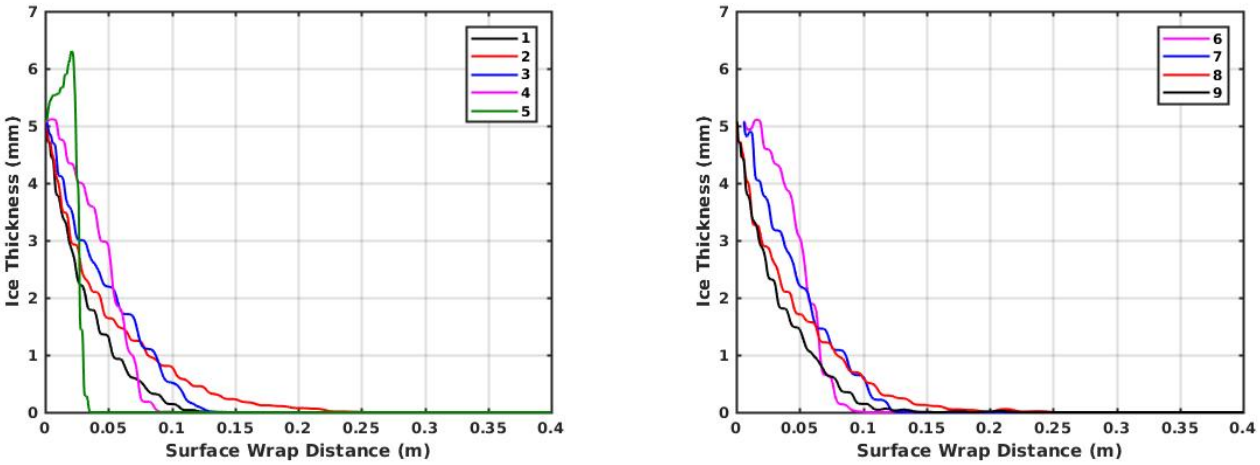


**Figure 27: The thickness of the ice accreted, predicted by GT-ICE, along the nine surface streamlines labeled under Figure 25.**

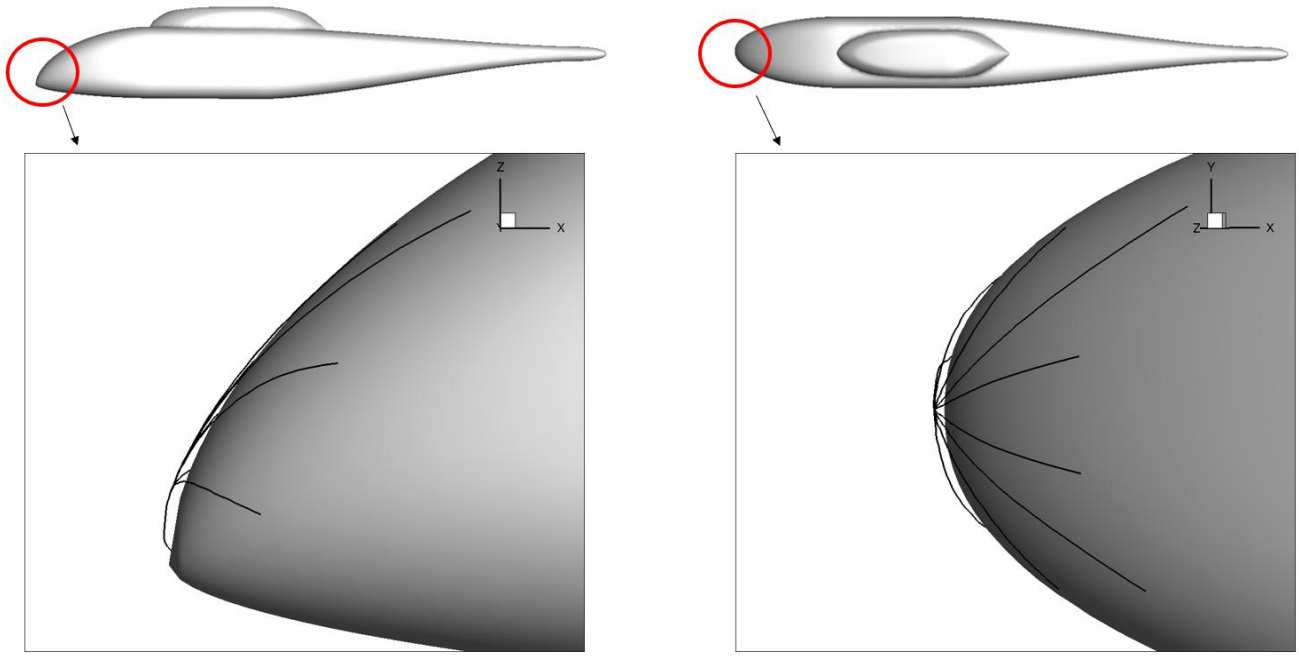


**Figure 28: A three-dimensional representation of the ice shape obtained using the ice thickness values predicted by GT-ICE, along the nine surface streamlines shown under Figure 25.**

## CONCLUDING REMARKS

A methodology to handle ice accretion on complex geometries was proposed. The existing extended Messinger solver developed at Georgia Tech, GT-ICE, was employed for modeling the ice accretion on a commercial transport airfoil, a swept wing and a helicopter fuselage. Unstructured grids were used for the flow field and droplet impingement calculations. Spatial marching along surface streamlines was carried out to include the effects of three-dimensional flow. Data interpolation, with regards to the flow field and the droplet impingement efficiency, along the streamlines was carried out using Tecplot. The computational predictions from GT-ICE were compared with experimental data, when available, and other computational codes such as LEWICE and STAR-CCM+.

For the commercial transport airfoil case, good agreement with the experimental data is observed. GT-ICE predicts thicker ice close to the leading edge, compared to the experimental data, however the extents of the ice formation are well predicted.

For the MS(1)-317 swept wing case, no experimental data for ice accretion was available, therefore, comparisons have been made with other computational codes: LEWICE3D and STAR-CCM+. GT-ICE and STAR-CCM+ predict similar ice shapes, whereas some differences with LEWICE3D predictions are observed. One of the reasons attributed for these are the impingement collection efficiency values.

For the final case of the Robin fuselage, no experimental data for icing was available, however ice accretion studies were carried out along nine different streamlines to demonstrate the validity of the methodology proposed. Ice accretion was only observed close to the nose of the fuselage. This is attributed to the high droplet impingement and coefficient of skin friction values close to the nose. The predicted ice thickness trails off sharply as the surface wrap distance from the nose increases.

Additional studies are necessary to further validate the proposed methodology. More cases such as those with ice horn formations and ones including the effects of rotor down wash will be investigated in future works.

## REFERENCES


1. Messinger, B. L., "Equilibrium Temperature of an Unheated Icing Surface as a Function of Air Speed," Journal of the Aeronautical Sciences, January. 1953, pp. 29–42.
2. Bourgault, Y., Boutanios, Z. Habashi, W., "FENSAP-ICE's Three-Dimensional In-Flight Ice Accretion Module, ICE3D", Journal of Aircraft, vol.37 no.1 (95-103) 2000.
3. Bourgault, Y., Beaugendre, H., and Habashi, W. G., "Development of a Shallow-Water Icing Model in FENSAP-ICE," Journal of Aircraft, Vol. 37, No. 4, 2000, pp. 640–646.
4. Habashi, W. G., Morency, F., and Beaugendre, H., "FENSAP-ICE: a comprehensive 3D Simulation Tool for In-flight Icing," 7th International Congress of fluid Dynamics and Propulsion, Sharm-El-Sheikh, Egypt, December 2001.
5. Beaugendre, H; Morency, F; Habashi, W G, "FENSAP-ICE's three-dimensional in-flight ice accretion module: ICE3D", Journal of Aircraft. Vol. 40, no. 2, pp. 239-247. Mar.-Apr. 2003.
6. Beaugendre, H., "A PDE-Based 3D Approach to In-Flight Ice Accretion," Ph.D. Thesis, McGill Univ., Montreal, June 2003.
7. Tran, P., Baruzzi, G. S., Akel, I., Habashi, W. G., and Narranmore, J. C., "FENSAP-ICE Applications to Complete Rotorcraft Configurations," SAE Transactions: Journal of Aerospace, Vol. 112, No. 1, 2003, pp. 1-13.
8. Fouladi, H., Habashi, W. G., and Ozcer, I. A., "Quasi-Steady Modeling of Ice Accretion on a Helicopter Fuselage in Forward Flight," Journal of Aircraft. Vol. 50, no. 4, pp. 1169-1178. July – August 2013.
9. Potapczuk, M. G., "LEWICE/E: An Euler Based Ice Accretion Code," NASA OH 105389, 1992.
10. Wright, W. B. and Rutkowski, A., "Validation Results for LEWICE 2.0," NASA CR 208690, Nov. 1998.
11. Wright, W. B., "User Manual for the NASA Glenn Ice Accretion Code LEWICE Version 2.0", NASA CR-1999- 209409, Dec. 1999.
12. Wright, W. B., "Validation Methods and Results for a Two-Dimensional Ice Accretion Code" Journal of Aircraft, Vol. 35, No, 5, Sept. 1999.
13. Wright, W. B., "User Manual for the NASA Glenn Ice Accretion Code LEWICE Version 2.2.2, NASA CR-2002- 211723, Aug. 2002.
14. Wright, W. B., "Validation Results for LEWICE 3.0", AIAA 2005-1243, Jan. 2005.
15. Wright, W. B., "User's Manual for LEWICE 3.2", NACA CR-2008-214255, Nov. 2008.
16. Bidwell, C. S., and Potapczuk, M. G., "Users Manual for the NASA Lewis Three-Dimensional Ice Accretion Code (LEWICE3D)," NASA TM 105974, December 1993.
17. Bidwell, C.S., and Mohler Jr, S. R., "Collection Efficiency and Ice Accretion Calculations for a Sphere, a Swept MS(1)-317 Wing, a Swept NACA-0012 Wing Tip, an Axisymmetric Inlet, and a Boeing 737-300 Inlet," American Institute of Aeronautics and Astronautics 33rd Aerospace Sciences Meeting Exhibit, Reno, Nevada, January 1995.
18. Myers, T. G., "Extension to the Messinger Model for Aircraft Icing," AIAA Journal, Vol. 39, (2), February. 2001, pp. 211–218.
19. Kim, J., "Development of a Physics Based Methodology for the Prediction of Rotor Blade Ice Formation," Ph.D. Dissertation, Georgia Institute of Technology, 2015.
20. Kim, J., Sankar, L., and Kreeger, R. E., "Assessment of Classical Extended Messinger Models for Modeling Rotorcraft Icing Phenomena," Proceedings of the 40th European Rotorcraft Forum, September 2014.
21. Gupta, A., Sankar, L. N., Halloran, E., Palacios, J., and Kreeger, R. E., "Development and Validation of Physics Based Models for Ice Shedding," Proceedings of the 44th European Rotorcraft Forum, September 2018.
22. Gupta, A., Sankar, L. N., and Kreeger, R., "Modeling Ice Accretion: Full Integration into Navier-Stokes Solver", Vertical Flight Society 75th Annual Forum and Technology Display, Philadelphia, PA, May 2019.
23. STAR-CCM+ Tutorials, "Multiphase Flow – Dispersed Multiphase: Airfoil Icing", 2019.
24. Jones, W.P., and Launder, B. E., "The Prediction of Laminarization with a Two-Equation Model of Turbulence", International Journal of Heat and Mass Transfer, 15, pp. 301-314, 1972.

25. Rodi, W., “Experience with Two-Layer Models Combining the k-e Model with a One-Equation Model Neat the Wall,” American Institute of Aeronautics and Astronautics 29th Aerospace Sciences Meeting, Reno, Nevada, January 1991.
26. Spalart, P. R., and Allmaras, S. R., “A One-Equation Turbulence Model for Aerodynamic Flows”, American Institute of Aeronautics and Astronuatics-92-0439, 1992.
27. Schiller, L., and Naumann, A., “Uber die grundlegenden Berechnungen bei der Schwerkraftaufbereitung”, VDI Zeits, 77(12), pp. 318-320, 1933.
28. Ranz, W. E., and Marshall, W. R., “Evaporation from drops—Parts I and II”, Chemical Engineering Progress, 48(3), p. 141, 1952.
29. Addy Jr, H. E., “Ice Accretions and Icing Effects for Modern Airfoils”, NASA/TP – 2000-210031.
30. Freeman, C. E., and Mineck, R. E., “Fuselage Surface Pressure Measurements of a Helicopter Wind-Tunnel Model with a 3.15 Meter Diameter Single Rotor”, NASA-TM-80051, 1979.
31. Tecplot, Inc. “Tecplot 360 EX 2019 Release 1: User’s Manual”, Bellevue, Washington, 2019.

## AUTHOR CONTACT

Avani Gupta agupta354@gatech.edu, Lakshmi N. Sankar lakshmi.sankar@aerospace.gatech.edu, Richard E. Kreeger richard.e.kreeger@nasa.gov

## ACKNOWLEDGEMENTS

This research was partially funded by the Government under Agreement No. W911W6-17-2-0002. The U.S. Government is authorized to reproduce and distribute reprints for Government purposes notwithstanding any copyright notation thereon. The views and conclusions contained in this document are those of the authors and should not be interpreted as representing the official policies, either expressed or implied, of the Aviation Development Directorate or the U.S. Government.